Opsins are Phospholipid Scramblases in All Domains of Life

Zachary A. Maschmann[1,*], David E. Hardy[1], Indu Menon[2], Jenna Webb[1], Anant K. Menon[2] and Katrina T. Forest[1#]

[1]*Department of Bacteriology, University of Wisconsin–Madison, Madison, WI 53706*

[2]*Department of Biochemistry, Weill Cornell Medical College, New York, NY 10065*

#For Correspondence: Katrina T. Forest, forest@bact.wisc.edu

*ZAM current address: Department of Molecular Biology, Princeton University 08540

Running Title: Bacterial Opsins are Scramblases

Competing interests: The authors declare that no competing interests exist.

Abstract

Opsins are highly abundant retinal proteins in the membranes of photoheterotrophic bacteria. However, some microbial genomes encode an *opsin* but lack the gene for the final enzyme in retinal synthesis. To account for this paradox, we hypothesized that bacterial opsins play a role in membrane structure and/or biogenesis independent from their potential for light-driven signaling or proton pumping. After purifying actinorhodopsin from a cell-free expression system and from *E. coli* membranes upon overexpression, we demonstrated both *in vitro* and *in silico* that actinorhodopsin from *Nanopelagicus ca*. is a phospholipid

scramblase, serving in its pentameric state as a retinal-independent phospholipid diffusion channel. Phospholipid headgroups move along a transbilayer path between actinorhodopsin protomers, to equilibrate lipid content in the inner and outer leaflets. Two profound activities, membrane biosynthesis and capture of light energy, are thus facilitated by one ancient bacterial polypeptide. Light-dependent activity and light-independent phospholipid scrambling are shared functions of eukaryotic, archaeal, and bacterial rhodopsins.

Importance

Cells are surrounded by membranes which concentrate metabolites and protect cellular contents. Most biomembranes are phospholipid bilayers, in which the phospholipids of each leaflet orient their greasy tails inward and polar groups outward. Bilayer biogenesis depends on phospholipids synthesized on the cytofacial side of the membrane reorienting to the extracellular membrane leaflet. This reorientation requires proteins, termed scramblases, and it was shown that rhodopsins -- 7-helix photoactive membrane proteins bound to the cofactor retinal -- from organisms as widely divergent as mammals and archaea possess scramblase activity. Now we conclusively demonstrate using purified proteins in laboratory membranes as well as computational approaches, that bacterial rhodopsins are also phospholipid scramblases. This work is important because it highlights a surprising commonality among bacteria, archaea and eukaryotes and because it shows that rhodopsins – ancient proteins found in the last universal common ancestor – manifest two seemingly unrelated biochemical functions in one protein.

Keywords: Actinorhodopsin, ActR, Bacteriorhodopsin, CGMD, Lipid scrambling, Membrane Biogenesis, Photoheterotrophy, Rhodopsin

Wordcount: Abstract 154, Text 5282

Introduction

Living cells engage in an ongoing process of self-construction. Phospholipid bilayer membranes separate the cellular interior from exterior, concentrate cytoplasmic contents, and protect cellular components. Membrane production is needed for cell division, and as part of turnover and repair processes (1). Phospholipids are synthesized in the cytoplasmic leaflet of biogenic membranes, such as the cytoplasmic membrane of bacteria and the endoplasmic reticulum (2). Reorientation of phospholipids between leaflets, *lipid scrambling,* is necessary for uniform growth of the bilayer but occurs too slowly to support life if unassisted (3–8). Biogenesis of all extant membrane bilayers requires a solution to this problem (9, 10), and evolution of this function likely would have provided ancient protocells with strong fitness benefits. Indeed, compartmentalization to support early life may have relied on the modularity and renewability of lipid bilayers (11, 12). Living cells use a facilitated lipid diffusion channel, termed a scramblase, to catalyze transbilayer phospholipid equilibration (10, 13–16). Scramblases are thought to shield the charged phospholipid head group from the hydrophobic bilayer interior to expedite lipid scrambling (10, 13–16).

In recent years, rhodopsins—well known for their photon capture based activities—have been shown to moonlight as scramblases. Menon and colleagues used a fluorescence-based assay to show that purified bovine rhodopsin exhibits scramblase activity when reconstituted into large unilamellar vesicles (17), accounting for previous observations that lipids scramble rapidly across photoreceptor disc membranes (18, 19). Scramblase activity was shown to be ATP-independent and constitutive, occurring in the absence of light or the

retinal chromophore. Subsequent work showed that an archaeal rhodopsin — bacteriorhodopsin (BR) from the archaeon *Halobacterium salinarum* — also had light-independent scramblase activity (20). This functional parallelism was not a foregone conclusion given that the mammalian visual sensory transducer rhodopsin and archaeal proton-pumping BR are found in anciently diverged organisms that differ greatly in membrane composition, architecture, metabolism, and environment.

Eubacterial rhodopsins have been known only since Sargasso Sea metagenomics efforts uncovered proton-pumping proteorhodopsins in marine bacteria in 2000 (21), followed by identification of opsin gene sequences in highly abundant nano-actinobacteria in fresh water (22). Like BR, these bacterial retinylidene opsins harness photon energy to pump protons across the membrane (23–25). Yet, notably, not all opsin-encoding bacteria carry genes for the complete enzymatic pathway to synthesize the retinal chromophore (23, 24). While retinal may be scavenged in some natural environments (26–28), the incomplete pathway nonetheless led us to hypothesize that actinobacterial opsins (ActR) may moonlight (29) and exhibit a second, retinal-independent function. Given that *actR* transcript levels in the natural environment are extremely high (23, 30), implying abundant protein levels, this function could be related to membrane structure and stability, echoing the fact that BR makes up 75% of the dry weight of *Halobacterium salinarum* purple membranes (31). Alternatively, given that bovine visual opsin and BR are identified scramblases (17, 20), we hypothesized that ActR and other bacterial opsins would also be phospholipid scramblases. This idea was bolstered by recent preliminary evidence of a

92 Gram-negative bacterial proteorhodopsin (ptqPR) from *Psychroflexus torquis* acting as a
93 scramblase (32).

94 We now show that ActR catalyzes interchange of phospholipid between bilayer
95 leaflets. The dual ActR functions of proton pump (23) and scramblase emphasize the
96 versatility of photoreceptor function and may provide a molecular connection between
97 photoheterotrophy and membrane biogenesis.

98

99 **Results**

100 *Large-scale synthesis of ActR in an in vitro transcription/translation system*

101 We synthesized ActR (*Nanopelagicus ca*. genome sequence L06) in a wheat-germ
102 extract translation system (33) with the inclusion of retinal in the translation reaction.
103 Purification by nickel affinity and size exclusion yielded a single ActR protein band, migrating
104 more rapidly (<25 kDa) than expected from its ~29 kDa molecular weight, and co-purifying
105 with a triplet of proteins identified by mass spectrometry as chaperones from the wheat
106 germ extract (Figure 1A). The protein was highly colored (Figure 1B) with peak absorbance at
107 544 nm—characteristic of a bacterial rhodopsin with Leucine at the tuning position, and in
108 agreement with our previous observations for bacterially produced ActR (23, 34) (Figure 1C).
109 Purity and homogeneity of ActR was further demonstrated by our ability to crystallize it using
110 a cubic lipidic phase (Figure 1B, bottom panel).

111

112 *ActR facilitates transbilayer phospholipid transport*

113 To determine the scramblase activity of ActR we used standard fluorescence-based
114 assays (Figures 1D,E) in which proteins are reconstituted into large unilamellar vesicles
115 containing a trace amount of a fluorescent phospholipid reporter, *e.g.* 4-Nitro-2,1,3-
116 benzoxadiazole phosphatidylcholine (NBD-PC) (17, 20, 35). To assay scrambling, the
117 vesicles are interrogated with topological probes – the dianion dithionite (Figure 1D), which
118 reacts with the NBD fluorophore to eliminate its fluorescence, and fatty acid-free BSA (Figure
119 1E) which captures NBD-PC molecules that desorb from the vesicle surface, resulting in
120 partial fluorescence quenching.

121 Treatment of protein-free vesicles with dithionite is expected to result in ~50%
122 fluorescence loss as NBD-PC molecules in the outer leaflet of the vesicles are modified
123 whereas those in the inner leaflet are protected (Figure 1D, top row). This is what is
124 experimentally observed (Figure 1F, trace labeled 'L' plateaus at 53%). However, when the
125 vesicles contain an active scramblase, rapid exchange of NBD-PC between the inner and
126 outer leaflets of the vesicle results in total loss of fluorescence as the entire complement of
127 NBD-PC becomes exposed to dithionite (Figure 1D, bottom row). We reconstituted two
128 different amounts of cell-free produced ActR via detergent-destabilization of preformed
129 liposomes. We also reconstituted bovine opsin (BO) as a positive control. As shown in Figure
130 1F, dithionite treatment of ActR proteoliposomes (ActR-5, ActR-15) showed a greater loss of
131 fluorescence than seen with empty vesicles (L), indicating that ActR has scramblase activity.
132 Addition of hydroxylamine, which disrupts the Schiff's base linkage to retinal, had no impact
133 on scrambling activity (data not shown).

134 The reconstitutions were done at a protein:phospholipid ratio of ~5 μg/μmol (ActR-5
135 and BO-5) or ~15 μg/μmol (ActR-15). As ActR is smaller than BO (~29 kDa vs ~40 kDa), it
136 would be expected to functionalize at least as many vesicles as BO when reconstituted at
137 ~5 μg/μmol. Yet, the data show that the extent of fluorescence reduction is not as great for
138 ActR-5 (73%) as for BO-5 (91%) when the proteins are similarly reconstituted (Figure 1F).
139 Even when 3x more ActR was reconstituted (ActR-15, Figure 1F), the extent of reduction was
140 ~84%. A possible explanation for the lower efficiency with which ActR reconstitutes is that
141 like other opsins (20, 36–38), ActR multimerizes, and protein multimerization *en route* to
142 reconstitution leads to a fraction of vesicles populated with trimers or monomers rather than
143 with functional pentameric ActR scramblases as discussed below.

144 The fluorescence decay traces for ActR and BO-containing vesicles are well fit with a
145 double-exponential decay function which represents a convolution of the dithionite
146 reduction reaction rate ($t_{1/2}$ ~12 s) and a slower scrambling rate. For BO-5, the slow phase
147 has $t_{1/2}$ ~40 s, whereas for ActR-5 and ActR-15, the $t_{1/2}$ values are ~400 and ~180 s,
148 respectively. These values suggest that ActR-mediated scrambling is somewhat slower
149 under these experimental conditions than that observed for BO.

150 To complement data generated using dithionite, we next used BSA as a topological
151 probe. For empty vesicles, ~30% fluorescence loss is expected, as NBD-PC from the outer
152 leaflet of the vesicles is quantitatively captured by BSA (Figure 1E, top row). This is because
153 when bound to BSA, the quantum efficiency of NBD-PC is ~60% lower than when the lipid is
154 in the membrane (8, 39). For scramblase-equipped vesicles, transbilayer exchange of NBD-
155 PC enables all NBD-PC molecules to be captured by BSA, resulting in ~60% expected

156 fluorescence loss. Figure 1G shows greater fluorescence loss in ActR-containing vesicles
157 compared with empty vesicles, consistent with their scramblase activity. As with the
158 dithionite assay, greater fluorescence reduction was seen with ActR-15 than with ActR-5,
159 and BO-5 vesicles showed close to the maximum expected fluorescence loss.
160
161 *Scramblase activity of ActR purified from E. coli*
162 As an orthogonal means to isolate ActR, and to avoid the co-purification of wheat germ
163 chaperones, we overexpressed the same ActR sequence in *E. coli*, induced expression and
164 added retinal concomitantly, and purified the protein using metal affinity and gel filtration
165 chromatographies. SDS-PAGE analysis revealed a single band running at the expected size
166 for an ActR monomer (Figure 1H), with a characteristic purple color (Figure 1I) and a
167 maximum absorbance at 544 nm (Figure 1J). On reconstitution into unilamellar vesicles, the
168 bacterially-produced protein also showed robust phospholipid scramblase activity,
169 measured using the dithionite assay (Figure 1D, 1K). Thus, whether produced in a cell-free
170 system or expressed in *E. coli*, ActR demonstrates scramblase activity.
171
172 *ActR oligomeric state observed by EM*
173 Bacterial opsins have been observed in monomeric, trimeric and pentameric
174 quaternary arrangements (37, 38, 40) as well as hexamers, although the latter may be due to
175 native signal peptide sequences included in heterologously expressed proteins (26, 41).
176 Extended helices and a 3-omega motif dictate the pentameric state of *Gloeobacter*
177 rhodopsin (42). As these secondary structures are also found in ActR, we expect it to be

178 pentameric. The multimer state of ActR may be important for both its light-dependent
179 proton-pumping and scramblase activities. We investigated the ActR oligomeric state at the
180 neutral pH under which the scramblase assays were carried out, using negative stain
181 transmission electron microscopy (TEM) and analytical size-exclusion chromatography. TEM
182 images indicate a heterogeneous mixture of ActR oligomers (Supplemental Figure 2) with
183 pentamers identified in single particle analysis (Figure 2A). Pentamers and trimers are both
184 present by SEC (Supplemental Figure 2), likely in equilibrium based on experimental
185 conditions. Moreover, we observed a shift from pentamer and trimer to trimer and monomer
186 at low pH (see further discussion in Supplemental Information). Given experimental
187 observations and the knowledge that native functional states and most common structural
188 assemblages of proton pumping and ion pumping bacterial rhodopsins are pentamers (26,
189 37, 40, 42, 43), we hypothesize that the pentameric state of ActR is the scramblase active
190 one.
191
192 *Coarse-grained molecular dynamics support ActR pentamer scramblase activity*
193 To support our laboratory-based observations that ActR is a lipid scramblase, we
194 employed coarse-grained molecular dynamics (CGMD) simulations over an extended time
195 window to assess scrambling activity of ActR in three oligomeric states. We used the
196 computational protocol of Li *et al.* (44) to determine the scrambling rate by counting the
197 number of phospholipid inversions in the membrane per unit time. Three replicates of an
198 ActR pentamer model in a dioleoylphosphatidylcholine (DOPC) membrane bilayer showed
199 ~4 scrambling events/μs (Figure 2B), consistent with rates calculated for archaeal BR (20).

The lipid inversion rate of two positive controls (scEMC3 with ~5 events/μs and VDAC1 dimer with ~8 events/μs) were consistent with results reported by Li *et al.* (44). In contrast, the ActR monomer, ActR trimer, and VDAC1 monomer displayed negligible scrambling activity (Figure 2B).

Lipid translocation by the ActR pentamer shows no directional bias and, although durations vary, on average the complete inversion takes on the order of 100 ns. Our model suggests that transbilayer phospholipid diffusion occurs at protomer interfaces in ActR and involves polar and aromatic residues that form a hydrophilic groove, consistent with the previously described credit card model (15). Side chains spanning the hydrophilic groove derive from α-helix 1 (α1) of one protomer and α3 and α4 of the adjacent protomer (Figure 2C,D,E).

The scrambling trajectory can be described in steps. First, lipids are recruited by polar residues near the bilayer surface. For example, Tyr161 and Tyr164 on α5 serve this role in the event depicted in Figure 2C. The phospholipid does not linger in these positions for more than a frame or two during the CGMD simulation, and from 20 scrambling events chosen for a deeper analysis (of total 138 observed), these residues come into play in only 1 or 2 of the events, respectively. Thus, the recruitment step is transient and many different side chains may be able to act at this step.

After this initial recruitment of the phospholipid, the heart of the scrambling mechanism takes place within the inter-subunit groove. The phosphate bead enters a lower pocket and contacts Tyr32 (75% of events) and Thr123 (95% of events) (Figure 2C,E). During

221 this step, the lipid tails may sample an equatorial orientation relative to the bulk lipid of the
222 membrane (Figure 2C, 411 ns & 420 ns panels). Subsequently, Phe21 (100% of 20 events)
223 passes the DOPC molecule from the lower to an upper pocket. Passage into and through this
224 second water-containing cavity formed by Asn17, Ser20, Tyr93 and Tyr137 (contacted in
225 90%, 95%, 40% and 85% of events, respectively) is slow, with variable contact times on the
226 order of 10 ns for these residues (Figure 2C-F). The buried water molecules are displaced
227 from this major pocket when the PO4 bead enters. All of these transitions can include
228 backsliding. The upper cavity is formed by side chains from three helices at the oligomer
229 interface; Asn17 on α1 of one monomer interacts with Tyr93 on α3 and Tyr137 of α4 from the
230 adjacent monomer (Figure 2C,E).

231 Finally, an additional step involves transient contact with surface residues (for
232 example, Gln11 and Asn220), after which the lipid diffuses into the bulk membrane.

233 *Retinal does not affect scrambling in silico but polar residue substitutions along cleft do*

234 ActR scramblase activity is not changed in laboratory experiments with the addition
235 of hydroxylamine, nor was illumination part of our protocol. Retinal was not present in our
236 CGMD simulations. Thus, scramblase activity of ActR does not depend on chromophore or
237 light. Nonetheless, to assess whether retinal has an effect on scrambling rates *in silico*, we
238 built a simplified bead model of retinal and included it in additional computational tests of
239 scramblase activity (Supplemental Figure 2). The scrambling rate was not markedly different
240 in these MD simulations from those without retinal.

241 In order to computationally evaluate the importance of the α1 and α4 polar amino
242 acids as core elements of the scrambling groove, we created four ActR variants with two
243 substitutions each and tested their scrambling activity as described above for the native
244 sequence. Consistent with the identification of polar residues in the cleft as major contact
245 points for the PO4 bead, both our double substitutions N17L/Y137F and N17L/T123L
246 showed a reduced scrambling of ~1 event/μs (Supplemental Figure 2).
247

248 **Discussion**

249 Moonlighting is common among identified scramblases — multiple scrambling
250 GPCRs (36, 45) and TMEM16 (46) in eukaryotes, numerous bacterial, ER, and mitochondrial
251 membrane insertases (44, 47), and Gram positive (this work), Gram negative (32) and
252 archaeal rhodopsins (20) perform other functions including ion transport, protein
253 translocation, and signal transduction. Members of the TMEM16 family of proteins, for
254 example, function either as chloride channels or as nonspecific ion channels/lipid
255 scramblases. The chloride channel members of this family may have derived from a
256 primordial scramblase and evolved chloride transport at the expense of scramblase
257 activity (48). It appears likely that yet-to-be discovered scramblases moonlight with other
258 functions. The ubiquitous nature of scramblase activity in diverse membrane proteins also
259 helps explain why it has been difficult to pinpoint a unique and essential scramblase in
260 some organisms (5).

261 Rhodopsins were ancient proteins found in early-Earth life forms (49, 50), suggesting
262 they could have functioned as scramblases in the earliest cells. In the modern world,

263 microbial rhodopsins are found across Bacteria, Archaea, and even some giant viruses (51,
264 52), with phylogenetic evidence suggesting that this wide distribution is due, at least in part,
265 to frequent horizontal gene transfer (53). We are not aware of any conserved sequence
266 motifs linked to the scramblase functionality of rhodopsins across the domains of life. This
267 lack of sequence requirement suggests that scramblase functionality relies upon relatively
268 hydrophilic surface characteristics without selecting for specific residues. Moreover, we do
269 not expect opsin scramblase activity to be specific with respect to lipid head groups, as
270 known scramblases are promiscuous for their substrates but do not have unlimited
271 specificity for complex head groups (17, 54, 55). While scramblase activity is essential, the
272 molecular surface underpinning this function appears to be under low selective pressure,
273 possibly owing to the high rates of lipid scrambling exhibited by even rudimentary
274 scramblases (56, 57) that may render scramblases easily evolvable.

275 Our simulations show that the ActR pentamer exhibits robust scrambling activity,
276 consistent with our experiments showing that more ActR is needed to functionalize vesicles
277 in comparison to bovine opsin. As monomeric and trimeric forms of ActR showed nominal
278 scrambling, a fully functional, scrambling-competent hydrophilic groove is only present in
279 the pentameric form. The dependence of activity on oligomerization aligns with
280 observations from other scramblases such as VDAC1, where dimerization is necessary to
281 form a translocation-competent groove (39) and BR, where trimerization generates
282 interfaces that can scramble lipids (20).

283 The structural basis for actinorhodopsin-mediated scrambling centers on a
284 hydrophilic groove formed by helices 1 and 3+4 of neighboring protomers. This pathway is

285 lined with aromatic and polar residues that interact with the charged phospholipid
286 headgroup to facilitate translocation. The orientation of the phospholipid during the
287 scrambling event supports the credit-card insertion model, where the charged phosphate
288 head group slides between helices, forming transient interactions with polar groups, and
289 reorients in plane with the bulk lipid as it rejoins the bilayer (Figure 2C,D,F). Coarse-grained
290 resolution limits the precision with which we can observe side chain orientation and
291 hydrogen bonding. However, repeated observations of lipid contacts indicate a core set of
292 residues—including Asn17, Phe21, Tyr32, and Tyr137—that play a role in the translocation
293 mechanism.

294 We have shown that ActR from *Nanopelagicus ca*. of the acI lineage of actinobacteria
295 is a phospholipid scramblase, making it the third known microbial opsin with scramblase
296 activity alongside Gram-negative bacterial PtqPR and archaeal BR. Our demonstration of the
297 robust scrambling activity of Gram-positive bacterial actinorhodopsins supports the notion
298 that phospholipid scrambling is a fundamental function of rhodopsins across the domains
299 of life. This insight provides a broad foundation for further study of the scramblase/opsin
300 duality. Particularly intriguing open questions are 1) Is there a pH dependence of scrambling
301 activity? The oligomeric state of *Gloeobacter* rhodopsin has been shown to vary with pH (38)
302 and our size exclusion chromatography mirrors these results (Supplemental Figure 2).
303 Moreover, our computational results show that trimers don't scramble (Figure 2B), thus
304 providing a consistent model that the ActR low-pH oligomer is not an active scramblase.
305 Decreased scramblase activity at low pH would prevent dissipation of the proton gradient;
306 low phospholipid pKa values enable a scenario where outer leaflet phospholipids are

307 protonated and subsequently deprotonated when scrambled to the inner leaflet (58).
308 Though *Nanopelagicus ca*. primarily inhabits the fresh water epilimnion, a neutral pH
309 habitat, freshwater lakes and bogs can contain low pH zones that may provide
310 environmental pressure for a pH-dependent adaptation of scramblase activity by ActR (59).
311 Perhaps this is a common mechanism for regulating bacterial rhodopsin scramblase activity
312 with consequences for energetics as well as membrane biogenesis. 2) Does the secondary
313 antenna carotenoid associated with rhodopsin in many bacterial and archaeal opsins (23,
314 60–62) have an impact on scrambling? Further elucidation of the structural roles of
315 secondary carotenoids as well as scrambling mechanisms is necessary to understand the
316 interplay, if any, between antenna association and scramblase functionality. Although
317 carotenoid association may add to thermal stability (61), our experimental and
318 computational scrambling assays were all done in the absence of the actinorhodopsin
319 carotenoid (23) and thus we can confidently say the antenna is not required for scramblase
320 activity. 3) Is the earliest role of rhodopsin scrambling or photoheterotrophy, or did these
321 activities co-evolve? Using our CGMD pipeline, we evaluated the scramblase activity of a
322 plausible ancient opsin sequence recently proposed by ancestral sequence reconstruction
323 (49). We did not observe scramblase activity (data not shown). While this model has very
324 highly conserved residues associated with photoactivity, our current study concludes that
325 scramblase activity relies more subtly on appropriate alignment of amino acids with relevant
326 properties along a protomer interface than on invariant side chain identities. The study of the
327 evolution of scramblase activity in early opsins is an exciting area that warrants additional
328 analysis.

329 **Materials and Methods**

330 *Materials*

331 16:0-18:1 PC (POPC) (1-palmitoyl-2-oleoyl-glycero-3-phosphocholine), 16:0-18:1 PG
332 (POPG) (1-palmitoyl-2-oleoyl-sn-glycero-3-phospho-(1'-rac-glycerol) (sodium salt)), 16:0-
333 06:0 NBD PC (C6-NBD-PC) (1-palmitoyl-2-{6-[(7-nitro-2-1,3-benzoxadiazol-4-
334 yl)amino]hexanoyl}-sn-glycero-3-phosphocholine) and 14:0-06:0 NBD PC ((1-myristoyl-2-
335 {6-[(7-nitro-2-1,3-benzoxadiazol-4-yl)amino]hexanoyl}-sn-glycero-3-phosphocholine) were
336 purchased as chloroform solutions from Avanti® Polar Lipids. n-Dodecyl-B-D-maltoside
337 (DDM) was purchased from VWR International. Bio-Beads SM2 Adsorbents were purchased
338 from Bio-Rad. Amberlite XAD-2 and sodium dithionite were purchased from Sigma Aldrich,
339 and fatty acid-free BSA was from EMD Millipore. Gibson Assembly® Master Mix was
340 purchased from New England BioLabs. PhusionTM High-Fidelity DNA Polymerase
341 Transcription reaction components, including S6 RNA polymerase, NTPs, RNase inhibitor,
342 and buffer were purchased from Promega Corporation. Translation reaction components,
343 including WEPRO® 8240H, Creatine Kinase, and SUB-Amix, were purchased from CellFree
344 Sciences.

345 *Plasmid Construction*

346 DNA codon-optimized for expression in *E. coli* and encoding the amino acid
347 sequence of ActR ($ActR_{L06}$ from *Nanopelagicus* ca. single-cell amplified genome L06 (acI-B))
348 (63, 23) was cloned into a pEU-C-His flexiVector, chosen for its suitability for *in vitro* protein
349 production, under the transcriptional control of the SP6 promoter (33). Insertion of the

350 coding sequence for ActR extended with a C-terminal 6x-His tag into the pEU flexiVector was
351 performed by amplifying plasmid fragments using PCR followed by Gibson Assembly (64,
352 65). The same DNA sequence was also inserted behind the T7 promoter of a pET-28a vector
353 using Gibson Assembly for expression in *E. coli*. Amplification of DNA fragments was
354 performed using Phusion™ High-Fidelity DNA Polymerase. Gibson Assembly was performed
355 using Gibson Assembly® Master Mix. The molecular weight of the 6x-His-tagged ActR
356 monomer is 29.7 kDa, with a predicted pI of 8.64.

357 *Large Scale Cell Free ActR Production*

358 Large scale transcription and translation reactions were carried out essentially as
359 described in Aly *et al.* (33, 66) using low magnesium buffer (Cell Free Sciences) for
360 transcription. Briefly, ActR-His_6 protein was synthesized in a 12-ml 8240H wheat germ
361 extract cell-free translation system (Cell Free Sciences) at 60 OD, using 0.1% MNG-10
362 (maltose neopentyl glycol-10) with 0.02% cholesteryl hemisuccinate (CHS) buffer, and 0.1
363 mM all-trans retinal was added during the translation. ActR was purified by Ni-affinity
364 chromatography followed by size exclusion. Protein was concentrated to approximately 15
365 mg/ml in 10 mM Hepes pH 7.5, 100 mM NaCl, 0.3 mM TCEP, 0.05% DDM, 0.01% CHS and
366 stored at -80 C. The contaminating higher molecular weight bands were identified by mass
367 spectrometry to contain uncharacterized wheat protein with Uniprot ID BAK08004.1, NADH
368 Dehydrogenase, and HSP 90.

369 *ActR Expression and Purification in* E. coli

370 BL21 (DE3) *E. coli* cells were used for recombinant expression of ActR. 10 mL of an
371 overnight culture was used to inoculate 1 L of LB supplemented with 50 μg/mL kanamycin,
372 which was then incubated with shaking (37°C, 250 rpm) until the OD_{600nm} reached 0.3, at
373 which point the temperature was reduced to 22°C. At OD_{600nm} of 0.5-0.6, ActR expression
374 was induced by adding powdered IPTG to a final concentration of 0.5 mM. All-trans retinal
375 was added concomitantly to a final concentration of 9 μM from a 50 mg/mL stock solution in
376 ethanol. After 16-20 hrs of growth in the dark, the culture was centrifuged at 4,000 g for 12
377 minutes at 4°C. After a freeze-thaw cycle, cells were resuspended in lysis buffer (50 mM Tris,
378 300 mM NaCl, 5 mM $MgCl_2$, 130 μM $CaCl_2$, 1 mg/mL lysozyme, 1 mM PMSF, pH=7.40), and
379 sonicated. This and all subsequent steps were carried out at 4°C. The sample was clarified
380 at 10,000g for 20 min, after which the supernatant was centrifuged at 40,000g for 45 min to
381 pellet membranes. The membrane fraction was resuspended in 20 mL of solubilization
382 buffer (50 mM Tris, 300 mM NaCl, 5 mM $MgCl_2$, 130 μM $CaCl_2$, 10 mg/mL DDM, pH=7.40)
383 using a Potter homogenizer, and incubated with rocking in the dark for 16-20 hrs. Aggregates
384 were removed by centrifugation at 40,000g for 20 min. The supernatant (~20 mL), now
385 containing solubilized membrane proteins, was collected and flowed continuously over 5
386 mL of Ni-NTA resin at 1 mL/min for 16-20 hrs using a peristaltic pump. The Ni-NTA resin was
387 washed with >20 bed volumes of wash buffer (50 mM Tris, 300 mM NaCl, 50 mM Imidazole,
388 0.5 mg/mL DDM, pH=7.40) and ActR was eluted with wash buffer containing successively
389 higher imidazole concentrations, from 100 mM to 500 mM. ActR-containing fractions were
390 pooled, and concentrated along with DDM in a 10 kDa – cutoff spin concentrator (Millipore).
391 Samples were dialyzed against 50 mM HEPES, 150 mM NaCl, pH=7.4 and injected onto a

392 Superdex 200 Increase 10/300 GL size exclusion column pre-equilibrated with buffer
393 identical to the dialysis reservoirs supplemented with 0.5 mg/ml DDM using an ÄKTA pure™
394 chromatography system. ActR-containing fractions were pooled, concentrated to approx.
395 0.5 mg/ml and immediately used for liposome reconstitution. The overall yield was ~0.5
396 mg/L of bacterial culture.

397 *ActR Negative Stain EM*

398 ActR expressed in *E. coli* and purified through the metal affinity chromatography step
399 was kept at 4°C and used to prepare EM grids on the same day. CF200-CU grids were glow
400 discharged for 30 s at 15 mA on a Pelco easiGlow discharge system. 4 µL of sample (diluted
401 in elution buffer to 240, 80, 32, or 8 µg/mL) was applied to each grid for 1 minute before
402 blotting. Grids were washed 2x in 20 µL buffer, 2x in 20 µL 2% Uranyl acetate (UA), followed
403 by one minute incubation in 2% UA. All images were collected on a Talos L120c 120 keV
404 electron microscope using a Ceta CMOS detector at the University of Wisconsin–Madison
405 Cryo-EM Research Center.

406 *Reconstitution of ActR into liposomes*

407 Liposomes were prepared using a 9:1 (mol/mol) POPC/POPG mixture, spiked with 0.5%
408 16:0-06:0 NBD PC or 14:0-06:0 NBD PC. The lipid mixture was prepared from chloroform
409 stock solutions, dried under nitrogen or in a rotary evaporator, and then placed under
410 vacuum overnight at ambient temperature before being resuspended in buffer (50 mM
411 HEPES, 150 mM NaCl, pH 7.4) at a concentration of ~4 mg/mL. The resuspended lipids were
412 processed further and taken for ActR reconstitution using either of two methods as follows.

413 Method 1 (used for *E. coli*-produced ActR): The sample was bath sonicated for 5 min,
414 incubated at ambient temperature for 1 h, sonicated again and aliquoted for individual
415 reconstitution experiments. Each aliquot was incubated with DDM (0.5% final) at ambient
416 temperature for 1 h, rotating end-over-end. ActR was then added, and incubation continued
417 for 1 h. Reconstitution was achieved by adding washed Amberlite XAD-2 (150 mg) followed
418 by incubation at ambient temperature for 1 h with end-over-end rotation. The samples were
419 withdrawn and added to a fresh aliquot of Amberlite, followed by incubation overnight at 4°C
420 with end-over-end rotation. Following this, the samples were withdrawn and transferred to
421 tubes containing fresh Amberlite for a final incubation at ambient temperature for 1 h. The
422 resulting proteoliposomes were stored at 4°C for up to two days, diluted 1/10 in excess buffer
423 and passed through a 0.2 μm filter on a Hamilton syringe assembly to produce a narrow size
424 distribution of ActR-containing liposomes (67, 68). Method 2 (used for cell-free synthesized
425 ActR): The sample was extruded successively through 400 nm and then 200 nm filters as
426 described (39) to generate unilamellar vesicles with an average diameter of 170 nm. TX-100
427 (0.2% final) was added to destabilize the vesicles, before adding ActR. The mixture was
428 treated with one shot of washed BioBeads to remove detergent, initially at room
429 temperature and then overnight at 4°C. The resulting vesicles were assayed directly (no
430 further extrusion).

431 *Scramblase Assays*

432 Scramblase activity assays were performed as previously described (17, 20, 69, 70),
433 using vesicles diluted to 2.5 mL in buffer (50 mM HEPES, 150 mM NaCl, pH7.4). NBD
434 fluorescence (λ_{ex}=470 nm, λ_{em}=530 nm) was monitored over time in spectrofluorimeters

435 (QuantaMaster Model C-60/2000 or Horiba) equipped with a temperature-controlled
436 cuvette holder, with a magnetic stirring apparatus. After obtaining a stable fluorescence
437 signal, dithionite (from a 1 M stock) or fatty acid-free BSA (from a 75 mg/ml stock) was added.
438 Addition of dithionite (final 10-20 mM) covalently modifies the fluorescent NBD moiety and
439 eliminates its fluorescence signal (71), leading to fluorescence drops of 50-100% for protein-
440 free liposomes and scramblase-active proteoliposomes, respectively. BSA (final 15 mg/ml)
441 captures and quenches NBD-PC molecules that desorb from the outer leaflet, leading to
442 fluorescence drops of ~30-60% for protein-free liposomes and scramblase-active
443 proteoliposomes, respectively (8, 72).

444 Fluorescence traces were normalized to stable fluorescence emission values prior to
445 dithionite or BSA addition, and analyzed as described (73) using mono-exponential fits for
446 protein-free liposomes and a double-exponential fit for ActR-containing samples. Analyses
447 were performed within MATLAB or GraphPad Prism, using their curve fitting functions.

448

449 *CGMD*

450 An ActR monomer structural model was generated using Chai-1 for *de novo* structure
451 prediction (74). The crystal structure of VDAC1 (RCSB: 6G6U) and bovine opsin (RCSB:
452 4A4M) were obtained from the RCSB Protein Data Bank (75). For scEMC3, missing regions in
453 the crystal structure (6WB9) were modeled using AlphaFold3 (76, 77). Two BR dimers were
454 tested and compared; one generated in AlphaFold3 and aligned to a crystal structure (4MD2)
455 and the other a vacuum-minimized crystal structure (1AT9). We found similar scramblase
456 activity in both models, and herein we present the AI-predicted model. CGMD simulations

457 were performed on a high-throughput computing cluster using the HTCondor software suite
458 and GROMACS 2022.2 (78, 79). Visual Molecular Dynamics (VMD) and Tachyon were used
459 for trajectory visualization and image rendering (80, 81).

460 Protein models were initially subjected to energy minimization in a vacuum until the
461 maximum force on any atom was below 100 $kJ \cdot mol^{-1} \cdot nm^{-1}$. Both the minimization and
462 production runs were conducted using a GROMACS 2022.2 container image hosted on
463 Docker Hub. Following minimization, the ActR trimer and pentamer were built by aligning the
464 monomer to a trimeric *Halobacter salinarum* BR model (1AT9) (82) and to a pentameric
465 sodium-pumping rhodopsin (KR2) from *Dokdonia eikasta* (6YC3) which was
466 crystallographically determined at 2.1 Å resolution (37). VDAC1 monomers were aligned to
467 the anti-parallel dimer RCSB structure and subsequently manually adjusted to the highly
468 scramblase-active parallel conformation described by Jahn et al. (39).

469 Proteins were embedded in a dummy membrane using the Orientation of Proteins in
470 Membranes (OPM) web server (83). The resulting protein–membrane systems were built and
471 solvated using CHARMM-GUI, then converted to coarse-grained representations using the
472 Martini 3 force field with Elastic Network Dynamics (ElNeDyn) (84–88). Each membrane
473 leaflet contained 400–500 molecules of 1,2-dioleoyl-sn-glycero-3-phosphocholine (DOPC),
474 for a total of 800–1000 lipid molecules per bilayer. Electrostatic charges in the protein were
475 counterbalanced by adding Na^+ and Cl^- ions to solution to bring the net charge to zero. Each
476 system was solvated with approximately 2×10^4 water beads.

To profile lipid dynamics in the presence of putative scramblases, simulations consisted of energy minimization, equilibration, and a production run with randomized initial velocities. Production simulations were run for 5×10^8 steps with a time step of 20 fs, yielding a total trajectory length of 10 μs. Temperature was maintained at 310 K using a velocity-rescaling (v-rescale) thermostat within an NPT ensemble. Pressure was set to 1 bar using the Parrinello–Rahman barostat. Calculations were executed on a local GROMACS container and using HTCondor at the UW-Madison Center for High Throughput Computing (89).

Systems were interrogated for scramblase activity by measuring phosphate headgroup (PO_4) angles of every DOPC every 1 ns following the method described by Li *et al*. (44). A vector is defined whose direction bisects the angle between the two vectors from head group to lipid tail for each DOPC. A buffer region is defined from 55º to 125º and an event is measured if the vector goes from under 55º to over 125º (or *vice versa*). Denoising was accomplished by averaging angles over 50 ns windows and sampling this smoothed data every 25 ns. The number of scrambling events per microsecond were averaged across all replicates. Simulations for VDAC1, scEMC3, BO, and ActR trimer were run twice and all other models were run three times.

Acknowledgements

We thank Prof. Brian Fox and Dr. Emily Beebe of the UW-Madison Transmembrane Protein Center for *in vitro* production and purification of ActR, Dr. Takefumi Morizumi and Prof. Oliver Ernst (University of Toronto) for a sample of bovine opsin, and Prof. Katherine Henzler-Wildman, Dr. Vilius Kurauskas and Prof. Katherine McMahon for valuable expertise. We

thank the Landick and Kaçar labs at the University of Wisconsin–Madison for use of laboratory equipment. We thank Prof. Elizabeth R. Wright, Dr. Bryan Sibert, and Alex Cotton at the University of Wisconsin–Madison Cryo-EM Research Center for negative stain cryo-EM services.

Funding and Additional Information

Research was supported by the USDA (WIS03052 to KTF), Einstein Foundation Visiting Fellow Program (to KTF), the Human Frontier Science Program (Ref.-No: RGP009/2023 to AKM) and the National Science Foundation (Grant 2425586 to AKM and Graduate Research Fellowship Grant No. 2137424 to DEH). The Transmembrane Protein Center was funded by the NIH (1U54 GM094584 to Brian Fox). Some of the fluorescence data were obtained at the University of Wisconsin – Madison Biophysics Instrumentation Facility, which was established with support from the University of Wisconsin – Madison and grants BIR-9512577 (NSF) and S10 RR13790 (NIH).

514 **References**

515 1. Zhang Y-M, Rock CO. 2008. Membrane lipid homeostasis in bacteria. Nat Rev Microbiol
516 6:222–233.

517 2. Sanyal S, Menon AK. 2009. Flipping Lipids: Why an' What's the Reason for? ACS Chem
518 Biol 4:895–909.

519 3. McConnell HM, Kornberg RD. 1971. Inside-outside transitions of phospholipids in
520 vesicle membranes. Biochemistry 10:1111–1120.

521 4. Rothman JE, Kennedy EP. 1977. Rapid transmembrane movement of newly synthesized
522 phospholipids during membrane assembly. Proc Natl Acad Sci U S A 74:1821–1825.

523 5. Hrafnsdóttir S, Menon AK. 2000. Reconstitution and Partial Characterization of
524 Phospholipid Flippase Activity from Detergent Extracts of the Bacillus subtilis Cell
525 Membrane. J Bacteriol 182:4198–4206.

526 6. Hrafnsdóttir S, Nichols JW, Menon AK. 1997. Transbilayer Movement of Fluorescent
527 Phospholipids in Bacillus megaterium Membrane Vesicles. Biochemistry 36:4969–
528 4978.

529 7. Huijbregts RPH, de Kroon AIPM, de Kruijff B. 1996. Rapid transmembrane movement of
530 C6-NBD-labeled phospholipids across the inner membrane of *Escherichia coli*.
531 Biochim Biophys Acta BBA - Biomembr 1280:41–50.

8. Kubelt J, Menon AK, Müller P, Herrmann A. 2002. Transbilayer Movement of Fluorescent Phospholipid Analogues in the Cytoplasmic Membrane of Escherichia coli. Biochemistry 41:5605–5612.

9. Kol MA, de Kruijff B, de Kroon AIPM. 2002. Phospholipid flip-flop in biogenic membranes: what is needed to connect opposite sides. Semin Cell Dev Biol 13:163–170.

10. Pomorski TG, Menon AK. 2016. Lipid somersaults: Uncovering the mechanisms of protein-mediated lipid flipping. Prog Lipid Res 64:69–84.

11. Luisi PL, Walde P, Oberholzer T. 1999. Lipid vesicles as possible intermediates in the origin of life. Curr Opin Colloid Interface Sci 4:33–39.

12. Deamer DW. 1997. The first living systems: a bioenergetic perspective. Microbiol Mol Biol Rev 61:239–261.

13. Sebinelli HG, Syska C, Čopič A, Lenoir G. 2024. Established and emerging players in phospholipid scrambling: A structural perspective. Biochimie S0300-9084(24)00218–9.

14. Wang Y, Kinoshita T. 2023. The role of lipid scramblases in regulating lipid distributions at cellular membranes. Biochem Soc Trans 51:1857–1869.

15. Pomorski T, Menon AK. 2006. Lipid flippases and their biological functions. Cell Mol Life Sci CMLS 63:2908–2921.

16. Sakuragi T, Nagata S. 2023. Regulation of phospholipid distribution in the lipid bilayer by flippases and scramblases. Nat Rev Mol Cell Biol 24:576–596.

17. Menon I, Huber T, Sanyal S, Banerjee S, Barré P, Canis S, Warren JD, Hwa J, Sakmar TP, Menon AK. 2011. Opsin Is a Phospholipid Flippase. Curr Biol 21:149–153.

18. Hessel E, Herrmann A, Müller P, Schnetkamp PPM, Hofmann K-P. 2000. The transbilayer distribution of phospholipids in disc membranes is a dynamic equilibrium. Eur J Biochem 267:1473–1483.

19. Wu G, Hubbell WL. 1993. Phospholipid asymmetry and transmembrane diffusion in photoreceptor disc membranes. Biochemistry 32:879–888.

20. Verchère A, Ou W-L, Ploier B, Morizumi T, Goren MA, Bütikofer P, Ernst OP, Khelashvili G, Menon AK. 2017. Light-independent phospholipid scramblase activity of bacteriorhodopsin from Halobacterium salinarum. Sci Rep 7:9522.

21. Beja O, Aravind L, Koonin EV, Suzuki MT, Hadd A, Nguyen LP, Jovanovich SB, Gates CM, Feldman RA, Spudich JL, Spudich EN, DeLong EF. 2000. Bacterial rhodopsin: evidence for a new type of phototrophy in the sea. Science 289:1902–1906.

22. Sharma AK, Zhaxybayeva O, Papke RT, Doolittle WF. 2008. Actinorhodopsins: proteorhodopsin-like gene sequences found predominantly in non-marine environments. Environ Microbiol 10:1039–1056.

23. Dwulit-Smith JR, Hamilton JJ, Stevenson DM, He S, Oyserman BO, Moya-Flores F, Garcia SL, Amador-Noguez D, McMahon KD, Forest KT. 2018. acI Actinobacteria Assemble a Functional Actinorhodopsin with Natively Synthesized Retinal. Appl Environ Microbiol 84:e01678-18.

24. Keffer JL, Hahn MW, Maresca JA. 2016. Characterization of an Unconventional Rhodopsin from the Freshwater Actinobacterium Rhodoluna lacicola. J Bacteriol 197:2704–2712.

25. Nakamura S, Kikukawa T, Tamogami J, Kamiya M, Aizawa T, Hahn MW, Ihara K, Kamo N, Demura M. 2016. Photochemical characterization of actinorhodopsin and its functional existence in the natural host. Biochim Biophys Acta BBA - Bioenerg 1857:1900–1908.

26. Hirschi S, Lemmin T, Ayoub N, Kalbermatter D, Pellegata D, Ucurum Z, Gertsch J, Fotiadis D. 2024. Structural insights into the mechanism and dynamics of proteorhodopsin biogenesis and retinal scavenging. Nat Commun 15:6950.

27. Wu X, Jiang J, Hu J. 2013. Determination and occurrence of retinoids in a eutrophic lake (Taihu Lake, China): cyanobacteria blooms produce teratogenic retinal. Environ Sci Technol 47:807–814.

28. Jaffe AL, Konno M, Kawasaki Y, Kataoka C, Béjà O, Kandori H, Inoue K, Banfield JF. 2022. Saccharibacteria harness light energy using type-1 rhodopsins that may rely on retinal sourced from microbial hosts. ISME J 16:2056–2059.

589 29. Singh N, Bhalla N. 2020. Moonlighting Proteins. Annu Rev Genet 54:265–285.

590 30. Hamilton JJ, Garcia SL, Brown BS, Oyserman BO, Moya-Flores F, Bertilsson S,
591 Malmstrom RR, Forest KT, McMahon KD. 2017. Metabolic Network Analysis and
592 Metatranscriptomics Reveal Auxotrophies and Nutrient Sources of the Cosmopolitan
593 Freshwater Microbial Lineage acI. mSystems 2:10.1128/msystems.00091-17.

594 31. Corcelli A, Lattanzio VMT, Mascolo G, Papadia P, Fanizzi F. 2002. Lipid-protein
595 stoichiometries in a crystalline biological membrane: NMR quantitative analysis of the
596 lipid extract of the purple membrane. J Lipid Res 43:132–140.

597 32. Fang J, Zhang Y, Zhu T, Li Y. 2023. Scramblase activity of proteorhodopsin confers
598 physiological advantages to Escherichia coli in the absence of light. iScience
599 26:108551.

600 33. Aly KA, Beebe ET, Chan CH, Goren MA, Sepúlveda C, Makino S, Fox BG, Forest KT. 2013.
601 Cell-free production of integral membrane aspartic acid proteases reveals zinc-
602 dependent methyltransferase activity of the Pseudomonas aeruginosa prepilin
603 peptidase PilD. MicrobiologyOpen 2:94–104.

604 34. Mao J, Jin X, Shi M, Heidenreich D, Brown LJ, Brown RCD, Lelli M, He X, Glaubitz C.
605 2024. Molecular mechanisms and evolutionary robustness of a color switch in
606 proteorhodopsins. Sci Adv 10:eadj0384.

607 35. Ploier B, Menon AK. 2016. A Fluorescence-based Assay of Phospholipid Scramblase
608 Activity. J Vis Exp JoVE 54635.

36. Goren MA, Morizumi T, Menon I, Joseph JS, Dittman JS, Cherezov V, Stevens RC, Ernst OP, Menon AK. 2014. Constitutive phospholipid scramblase activity of a G Protein-coupled receptor*. Nat Commun 5:5115.

37. Kovalev K, Astashkin R, Gushchin I, Orekhov P, Volkov D, Zinovev E, Marin E, Rulev M, Alekseev A, Royant A, Carpentier P, Vaganova S, Zabelskii D, Baeken C, Sergeev I, Balandin T, Bourenkov G, Carpena X, Boer R, Maliar N, Borshchevskiy V, Büldt G, Bamberg E, Gordeliy V. 2020. Molecular mechanism of light-driven sodium pumping. Nat Commun 11:2137.

38. Morizumi T, Ou W-L, Van Eps N, Inoue K, Kandori H, Brown LS, Ernst OP. 2019. X-ray Crystallographic Structure and Oligomerization of Gloeobacter Rhodopsin. Sci Rep 9:11283.

39. Jahn H, Bartoš L, Dearden GI, Dittman JS, Holthuis JCM, Vácha R, Menon AK. 2023. Phospholipids are imported into mitochondria by VDAC, a dimeric beta barrel scramblase. Nat Commun 14:8115.

40. Iizuka A, Kajimoto K, Fujisawa T, Tsukamoto T, Aizawa T, Kamo N, Jung K-H, Unno M, Demura M, Kikukawa T. 2019. Functional importance of the oligomer formation of the cyanobacterial H+ pump Gloeobacter rhodopsin. Sci Rep 9:10711.

41. Soto-Rodríguez J, Baneyx F. 2019. Role of the signal sequence in proteorhodopsin biogenesis in E. coli. Biotechnol Bioeng 116:912–918.

42. Morizumi T, Ou W-L, Van Eps N, Inoue K, Kandori H, Brown LS, Ernst OP. 2019. X-ray Crystallographic Structure and Oligomerization of Gloeobacter Rhodopsin. Sci Rep 9:11283.

43. Ayoub N, Djabeur N, Harder D, Jeckelmann J-M, Ucurum Z, Hirschi S, Fotiadis D. 2025. Actinorhodopsin: an efficient and robust light-driven proton pump for bionanotechnological applications. Sci Rep 15:4054.

44. Li D, Rocha-Roa C, Schilling MA, Reinisch KM, Vanni S. 2024. Lipid scrambling is a general feature of protein insertases. Proc Natl Acad Sci 121:e2319476121.

45. Morra G, Razavi AM, Pandey K, Weinstein H, Menon AK, Khelashvili G. 2018. Mechanisms of lipid scrambling by the G protein-coupled receptor opsin. Struct Lond Engl 1993 26:356-367.e3.

46. Lee B-C, Menon AK, Accardi A. 2016. The nhTMEM16 Scramblase Is Also a Nonselective Ion Channel. Biophys J 111:1919–1924.

47. Bartoš L, Menon AK, Vácha R. 2024. Insertases scramble lipids: Molecular simulations of MTCH2. Struct Lond Engl 1993 32:505-510.e4.

48. Kalienkova V, Clerico Mosina V, Paulino C. 2021. The Groovy TMEM16 Family: Molecular Mechanisms of Lipid Scrambling and Ion Conduction. 16. J Mol Biol 433:166941.

645 49. Sephus CD, Fer E, Garcia AK, Adam ZR, Schwieterman EW, Kacar B. 2022. Earliest
646 Photic Zone Niches Probed by Ancestral Microbial Rhodopsins. Mol Biol Evol
647 39:msac100.

648 50. DasSarma S, Schwieterman EW. 2021. Early evolution of purple retinal pigments on
649 Earth and implications for exoplanet biosignatures. Int J Astrobiol 20:241–250.

650 51. Bryant DA, Frigaard N-U. 2006. Prokaryotic photosynthesis and phototrophy
651 illuminated. Trends Microbiol 14:488–496.

652 52. Pinhassi J, DeLong EF, Béjà O, González JM, Pedrós-Alió C. 2016. Marine Bacterial and
653 Archaeal Ion-Pumping Rhodopsins: Genetic Diversity, Physiology, and Ecology.
654 Microbiol Mol Biol Rev MMBR 80:929–954.

655 53. Sharma AK, Spudich JL, Doolittle WF. 2006. Microbial rhodopsins: functional versatility
656 and genetic mobility. Trends Microbiol 14:463–469.

657 54. Hankins MTK, Parrag M, Garaeva AA, Earp JC, Seeger MA, Stansfeld PJ, Bublitz M. 2025.
658 MprF from Pseudomonas aeruginosa is a promiscuous lipid scramblase with broad
659 substrate specificity. Sci Adv 11:eads9135.

660 55. Arndt M, Alvadia C, Straub MS, Clerico Mosina V, Paulino C, Dutzler R. 2022. Structural
661 basis for the activation of the lipid scramblase TMEM16F. Nat Commun 13:6692.

662 56. Nakao H, Tsujii T, Saito H, Ikeda K, Nakano M. 2025. Synergistic effects of hydrophilic
663 residues in the transmembrane region on lipid scrambling activity of dimeric helices.
664 Colloids Surf B Biointerfaces 251:114612.

665 57. Nakao H, Sugimoto Y, Ikeda K, Saito H, Nakano M. 2020. Structural Feature of Lipid
666 Scrambling Model Transmembrane Peptides: Same-Side Positioning of Hydrophilic
667 Residues and Their Deeper Position. J Phys Chem Lett 11:1662–1667.

668 58. Marsh D. 2013. Handbook of Lipid Bilayers, 2nd ed. CRC Press, Boca Raton.

669 59. Rohwer RR, Kirkpatrick M, Garcia SL, Kellom M, McMahon KD, Baker BJ. 2025. Two
670 decades of bacterial ecology and evolution in a freshwater lake. Nat Microbiol 10:246–
671 257.

672 60. Balashov SP, Imasheva ES, Boichenko VA, Antón J, Wang JM, Lanyi JK. 2005.
673 Xanthorhodopsin: A Proton Pump with a Light-Harvesting Carotenoid Antenna.
674 Science 309:2061–2064.

675 61. Chuon K, Shim J, Kang K-W, Cho S-G, Hour C, Meas S, Kim J-H, Choi A, Jung K-H. 2022.
676 Carotenoid binding in Gloeobacteria rhodopsin provides insights into divergent
677 evolution of xanthorhodopsin types. Commun Biol 5:1–8.

678 62. Tzlil G, Marín MDC, Matsuzaki Y, Nag P, Itakura S, Mizuno Y, Murakoshi S, Tanaka T,
679 Larom S, Konno M, Abe-Yoshizumi R, Molina-Márquez A, Bárcenas-Pérez D, Cheel J,
680 Koblížek M, León R, Katayama K, Kandori H, Schapiro I, Shihoya W, Nureki O, Inoue K,
681 Rozenberg A, Chazan A, Béjà O. 2025. Structural insights into light harvesting by

682 antenna-containing rhodopsins in marine Asgard archaea. Nat Microbiol 10:1484–
683 1500.

684 63. Garcia SL, McMahon KD, Martinez-Garcia M, Srivastava A, Sczyrba A, Stepanauskas R,
685 Grossart HP, Woyke T, Warnecke F. 2013. Metabolic potential of a single cell belonging
686 to one of the most abundant lineages in freshwater bacterioplankton. ISME J 7:137–
687 147.

688 64. Gibson DG, Young L, Chuang R-Y, Venter JC, Hutchison CA, Smith HO. 2009. Enzymatic
689 assembly of DNA molecules up to several hundred kilobases. Nat Methods 6:343–
690 345.

691 65. Heydenreich FM, Miljuš T, Jaussi R, Benoit R, Milić D, Veprintsev DB. 2017. High-
692 throughput mutagenesis using a two-fragment PCR approach. Sci Rep 7:6787.

693 66. Beebe ET, Makino S-I, Nozawa A, Matsubara Y, Frederick RO, Primm JG, Goren MA, Fox
694 BG. 2011. Robotic large-scale application of wheat cell-free translation to structural
695 studies including membrane proteins. New Biotechnol 28:239–249.

696 67. Dearden GI, Ravishankar V, Sakata K, Menon AK, Bergdoll L. 2024. Protocol for the
697 production and reconstitution of VDAC1 for functional assays. STAR Protoc 5:103240.

698 68. Ong SGM, Chitneni M, Lee KS, Ming LC, Yuen KH. 2016. Evaluation of Extrusion
699 Technique for Nanosizing Liposomes. 4. Pharmaceutics 8:36.

700 69. Brunner JD, Schenck S, Dutzler R. 2016. Structural basis for phospholipid scrambling in
701 the TMEM16 family. Curr Opin Struct Biol 39:61–70.

702 70. Malvezzi M, Chalat M, Janjusevic R, Picollo A, Terashima H, Menon AK, Accardi A. 2013.
703 Ca2+-dependent phospholipid scrambling by a reconstituted TMEM16 ion channel.
704 Nat Commun 4:2367.

705 71. McIntyre JC, Sleight RG. 1991. Fluorescence assay for phospholipid membrane
706 asymmetry. Biochemistry 30:11819–11827.

707 72. Chang Q, Gummadi SN, Menon AK. 2004. Chemical Modification Identifies Two
708 Populations of Glycerophospholipid Flippase in Rat Liver ER. Biochemistry 43:10710–
709 10718.

710 73. Menon I, Sych T, Son Y, Morizumi T, Lee J, Ernst OP, Khelashvili G, Sezgin E, Levitz J,
711 Menon AK. 2024. A cholesterol switch controls phospholipid scrambling by G protein-
712 coupled receptors. J Biol Chem 300:105649.

713 74. Team CD, Boitreaud J, Dent J, McPartlon M, Meier J, Reis V, Rogozhonikov A, Wu K. 2024.
714 Chai-1: Decoding the molecular interactions of life. bioRxiv
715 https://doi.org/10.1101/2024.10.10.615955.

716 75. Razeto A, Gribbon P, Loew C. 2019. The dynamic nature of the VDAC1 channels in
717 bilayers: human VDAC1 at 2.7 Angstrom resolution: 6g6u.

718 76. Abramson J, Adler J, Dunger J, Evans R, Green T, Pritzel A, Ronneberger O, Willmore L,
719 Ballard AJ, Bambrick J, Bodenstein SW, Evans DA, Hung C-C, O'Neill M, Reiman D,
720 Tunyasuvunakool K, Wu Z, Žemgulytė A, Arvaniti E, Beattie C, Bertolli O, Bridgland A,
721 Cherepanov A, Congreve M, Cowen-Rivers AI, Cowie A, Figurnov M, Fuchs FB,
722 Gladman H, Jain R, Khan YA, Low CMR, Perlin K, Potapenko A, Savy P, Singh S, Stecula
723 A, Thillaisundaram A, Tong C, Yakneen S, Zhong ED, Zielinski M, Žídek A, Bapst V, Kohli
724 P, Jaderberg M, Hassabis D, Jumper JM. 2024. Accurate structure prediction of
725 biomolecular interactions with AlphaFold 3. Nature 630:493–500.

726 77. Bai L, You Q, Feng X, Kovach A, Li H. 2020. Structure of the ER membrane complex, a
727 transmembrane-domain insertase. Nature 584:475–478.

728 78. Bekker H, Berendsen HJC, Djikstra EJ, Achterop S, van Drunen R, van der Spoel D,
729 Sijbers A, Keegstra H. 1993. Gromacs: A parallel computer for molecular dynamics
730 simulations, p. 252–256. *In* de Groot, RA, Nadrchal, J (eds.), Physics Computing '92.
731 World Scientific, Singapore.

732 79. Thain D, Tannenbaum T, Livny M. 2005. Distributed computing in practice: the Condor
733 experience. Concurr - Pract Exp 17:323–356.

734 80. Humphrey W, Dalke A, Schulten K. 1996. VMD: Visual molecular dynamics. J Mol Graph
735 14:33–38.

736 81. Stone J. 1998. An Efficient Library for Parallel Ray Tracing and Animation. Computer
737 Science Department, University of Missouri-Rolla.

738 82. Kimura Y, Vassylyev DG, Miyazawa A, Kidera A, Matsushima M, Mitsuoka K, Murata K,
739 Hirai T, Fujiyoshi Y. 1997. Surface of bacteriorhodopsin revealed by high-resolution
740 electron crystallography. Nature 389:206–211.

741 83. Lomize MA, Pogozheva ID, Joo H, Mosberg HI, Lomize AL. 2012. OPM database and
742 PPM web server: resources for positioning of proteins in membranes. Nucleic Acids
743 Res 40:D370-376.

744 84. Jo S, Kim T, Iyer VG, Im W. 2008. CHARMM-GUI: A web-based graphical user interface
745 for CHARMM. J Comput Chem 29:1859–1865.

746 85. Brooks BR, Brooks III CL, Mackerell Jr. AD, Nilsson L, Petrella RJ, Roux B, Won Y,
747 Archontis G, Bartels C, Boresch S, Caflisch A, Caves L, Cui Q, Dinner AR, Feig M,
748 Fischer S, Gao J, Hodoscek M, Im W, Kuczera K, Lazaridis T, Ma J, Ovchinnikov V, Paci
749 E, Pastor RW, Post CB, Pu JZ, Schaefer M, Tidor B, Venable RM, Woodcock HL, Wu X,
750 Yang W, York DM, Karplus M. 2009. CHARMM: The biomolecular simulation program. J
751 Comput Chem 30:1545–1614.

752 86. Lee J, Cheng X, Swails JM, Yeom MS, Eastman PK, Lemkul JA, Wei S, Buckner J, Jeong
753 JC, Qi Y, Jo S, Pande VS, Case DA, Brooks CLI, MacKerell ADJr, Klauda JB, Im W. 2016.
754 CHARMM-GUI Input Generator for NAMD, GROMACS, AMBER, OpenMM, and
755 CHARMM/OpenMM Simulations Using the CHARMM36 Additive Force Field. J Chem
756 Theory Comput 12:405–413.

87. Qi Y, Ingólfsson HI, Cheng X, Lee J, Marrink SJ, Im W. 2015. CHARMM-GUI Martini Maker for Coarse-Grained Simulations with the Martini Force Field. J Chem Theory Comput 11:4486–4494.

88. Hsu P-C, Bruininks BMH, Jefferies D, Cesar Telles de Souza P, Lee J, Patel DS, Marrink SJ, Qi Y, Khalid S, Im W. 2017. CHARMM-GUI Martini Maker for modeling and simulation of complex bacterial membranes with lipopolysaccharides. J Comput Chem 38:2354–2363.

89. Center for High Throughput Computing. (2006). doi:10.21231/GNT1-HW21

766 **Figure Legends**

767 **Figure 1.** acI-B (*Nanopelagicus* ca.) ActR expressed in a cell free system or in *E. coli* is a
768 phospholipid scramblase

769 (A/H) SDS-PAGE analysis of affinity-purified (A) cell free- or (H) *E. coli*-produced ActR
770 following size-exclusion chromatography. (B/I) Image of (B) cell free- or (I) *E. coli*-produced
771 ActR showing strong reddish color. (C/J) Absorbance spectrum of (C) cell free- or (G) *E. coli*-
772 produced ActR. Note maximum absorbance at 543 nm.

773 (D) Protein free liposomes (L) and scramblase-containing proteoliposomes (P) are shown
774 schematically. The vesicles are prepared with a trace quantity of NBD-PC distributed equally
775 between inner and outer leaflets. Upon addition of dithionite, the nitro group in NBD-PC is
776 covalently modified to an amino group and the resulting ABD-PC is non-fluorescent.
777 Liposomes retain fluorescence signal from NBD-PC in the inner leaflet as dithionite cannot
778 enter the vesicles; for scramblase-containing proteoliposomes, lipids in the inner and outer
779 leaflets exchange and fluorescence decays further as NBD-PC molecules in the inner leaflet
780 reach the outer leaflet where they are modified by dithionite.

781 E) As in D), except that fatty-acid free BSA is used as a topological probe. NBD-PC molecules
782 that desorb from the outer leaflet of the outer membrane are captured by BSA. In complex
783 with BSA, NBD-PC fluorescence is ~60% lower than when the lipid is in the membrane.

784 F/G/K) Normalized time course scramblase assay data for (F/G) cell free- or (K) *E. coli*-
785 produced ActR. Dithionite or BSA was added at the indicated time point. Error bars in panel
786 G represent standard deviation of duplicate measurements, data in panels F/G represent

787 one of 3 independent experiments carried out under different proteoliposome reconstitution
788 conditions, and data in panel K represent one of 4 independent experiments.
789 Proteoliposomes were generated using ActR or bovine opsin (BO) at different
790 protein/phospholipid ratios (units of μg/μmol) as indicated on the trace labels, e.g. ActR-5
791 and ActR-15 represent samples with protein/phospholipid ratios of 5 and 15, respectively.

792 **Figure 2**. ActR is a Pentamer that Facilitates Scrambling as Assessed Computationally

793 A) Array of four representative negative stain electron microscopy images of ActR at
794 pH=7.4, and superposition of representative ActR TEM image over predicted ActR
795 pentameric structure.
796 B) CGMD scramblase events/μsecond accompanied by structural images. The upper
797 right inset shows the angles (in orange) in which rotations were not counted as
798 scrambling events.
799 C) CGMD scramblase "flip book" images of one DOPC moving through cleft and re-
800 orienting lipid tails. Those beads which were within 5 Å of the phosphate bead in any
801 frame are shown in green, PO4 bead is red, and lipid tail beads are blue.
802 D) One snapshot from the trajectory represented in part C is shown with beads from
803 each opsin monomer shaded differently to highlight the inter-protomer location of
804 the groove. Green protein beads are all those within 5 Å of the red phosphate bead (in
805 this frame representing atoms from N17, S20, F21 and Y93), while blue beads depict
806 the lipid tail.
807 E) Ribbon diagram of two adjacent protomers that form the scrambling groove, with side
808 chains in the groove that interact with lipids during scrambling labeled, and

occasionally observed interactions circled but not labeled. Each monomer is colored in a reverse rainbow from blue -> red as the chain progresses from N -> C terminus. Additionally, the left chain has a salmon interior surface while the right chain has a light blue interior surface, with visible α helices labeled on both chains.

F) Z-axis height above or below the center of the membrane for the PO4 bead as a function of time during passage through the cleft of the example individual DOPC shown in panel C. Dwell times for Y32, F21, and Y137 depicted as colored bars.

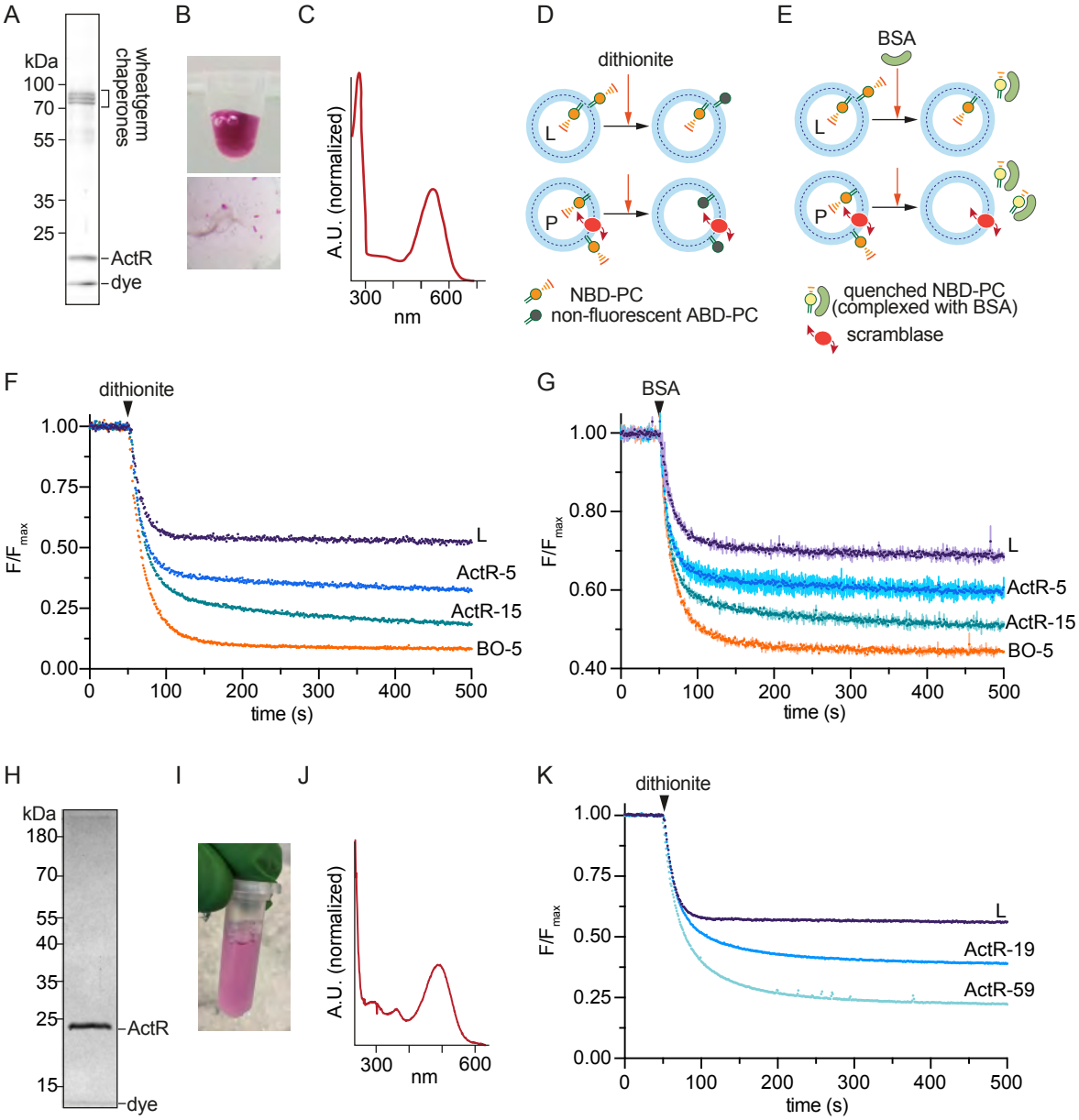

Maschmann et al., Fig 1

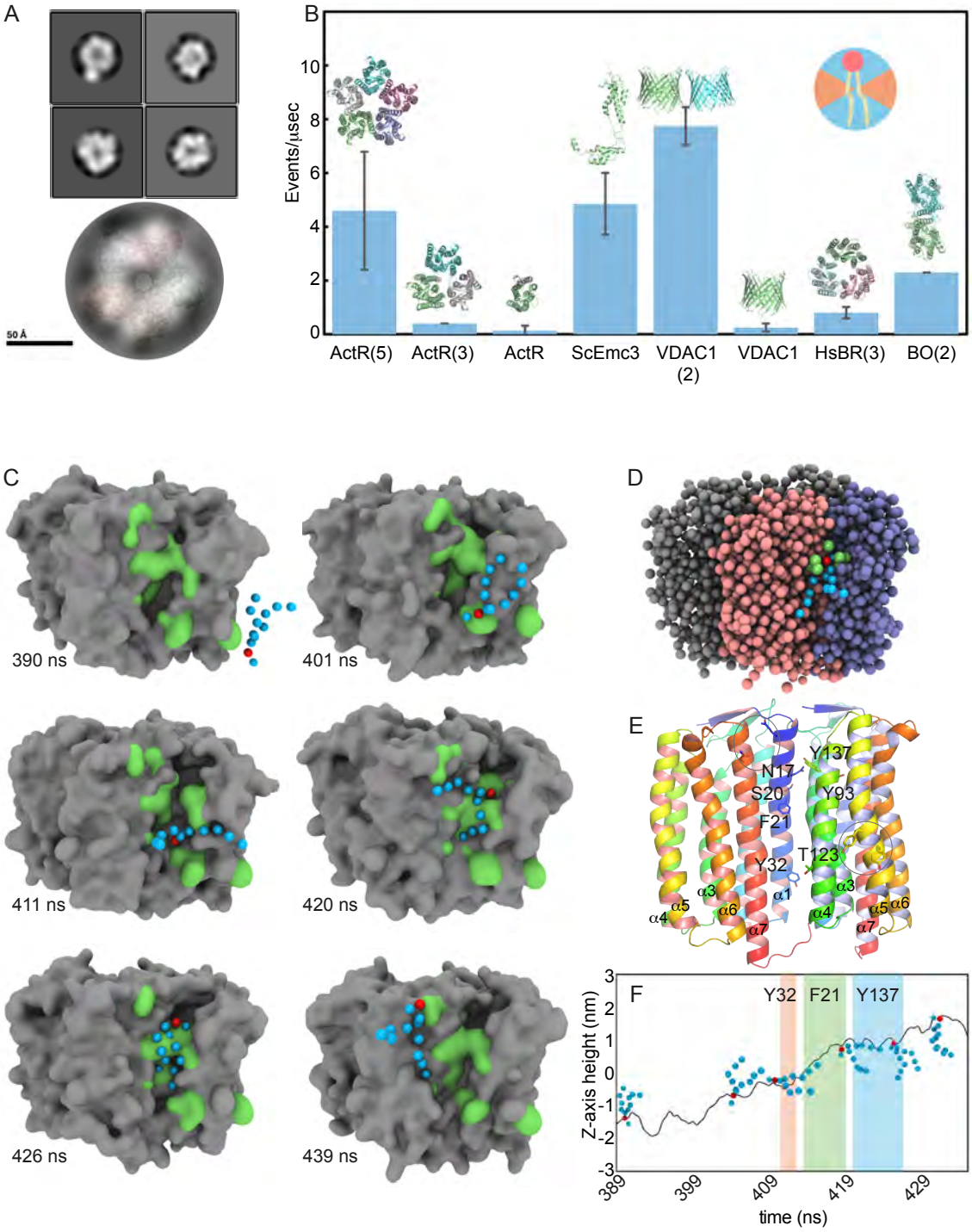

Maschmann et al., Fig 2

Supplemental Information for Opsins are Scramblases in All Domains of Life
Maschmann *et al.,* 2025

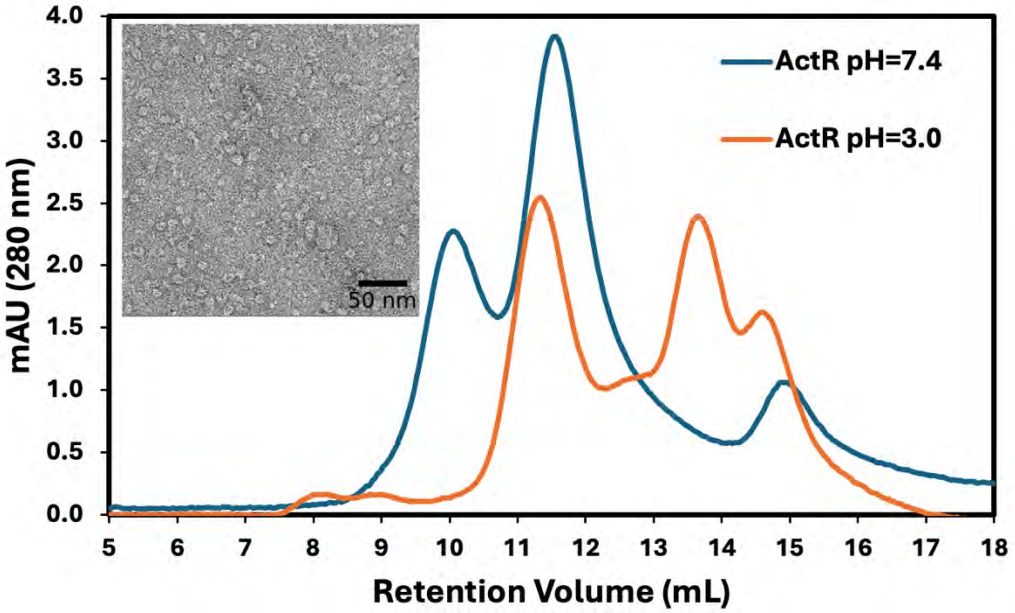

Supplemental Figure 1: ActR forms Pentamers at Neutral pH. ActR protein purified by nickel affinity was used for negative stain EM (inset shows grid area, isolated particles shown in Figure 2) and was run on an S200 Increase 10/300 GL SEC column at either pH 7.4 or 3.0. The peak at ~10 mL in the pH 7.4 trace is consistent with pentameric ActR. The oligomer equilibrium shifts to trimer and monomer at low pH, which is similar to behaviour reported for *Gloeobacter* rhodopsin (1).

ActR pentamer equilibrium is a function of pH

We investigated the oligomeric state of ActR and possible pH-dependent changes to this assembly using analytical size-exclusion chromatography (SEC). At pH=7.4, ActR predominantly assumes two oligomeric states as resolved by SEC (**Suppl Figure 2**). Based on expected retention volumes of soluble protein standards provided by Cytiva, these SEC peaks are consistent with pentameric and trimeric ActR. Furthermore, ActR changes the distribution of its oligomeric states at pH=3.0 (**Suppl Figure 2**), where the higher molecular weight, presumably pentameric, ActR peak disappears and ActR assumes a primarily trimeric state with a smaller molecular weight peak, possibly monomeric or dimeric ActR. Corollary experiments at pH=5.0 reveal similar SEC traces to those at pH=3.0 (not shown), consistent with the notion that the protonation state of a surface-exposed histidine residue such as H61 is responsible for controlling the stability of states. The mixture of oligomers at both pH=7.4 and pH=3.0 indicate that an equilibrium exists among oligomeric states of ActR. Stable oligomers ordinarily elute from a size-exclusion column in relatively narrow peaks. Contrariwise, ActR at all examined pH values exhibits relatively broad SEC elution peaks, suggesting that ActR oligomers exchange subunits over the course of size-exclusion.

To verify the pentameric state at neutral pH, electron microscopy images were taken of ActR following nickel affinity chromatography, and indicate a heterogeneous mixture of ActR oligomers (**Suppl Figure 2**). As the protonation state of H61 likely modulates the equilibrium of ActR oligomers with pH, the presence of imidazole in the sample probably effects the heterogeneity of conformations observed for ActR multimers. Nevertheless, ActR pentamers can be easily observed (**Figure 2**) and representative negative stain SEM images fit the profile of an AlphaFold2 model of pentameric ActR (**Figure 2**).

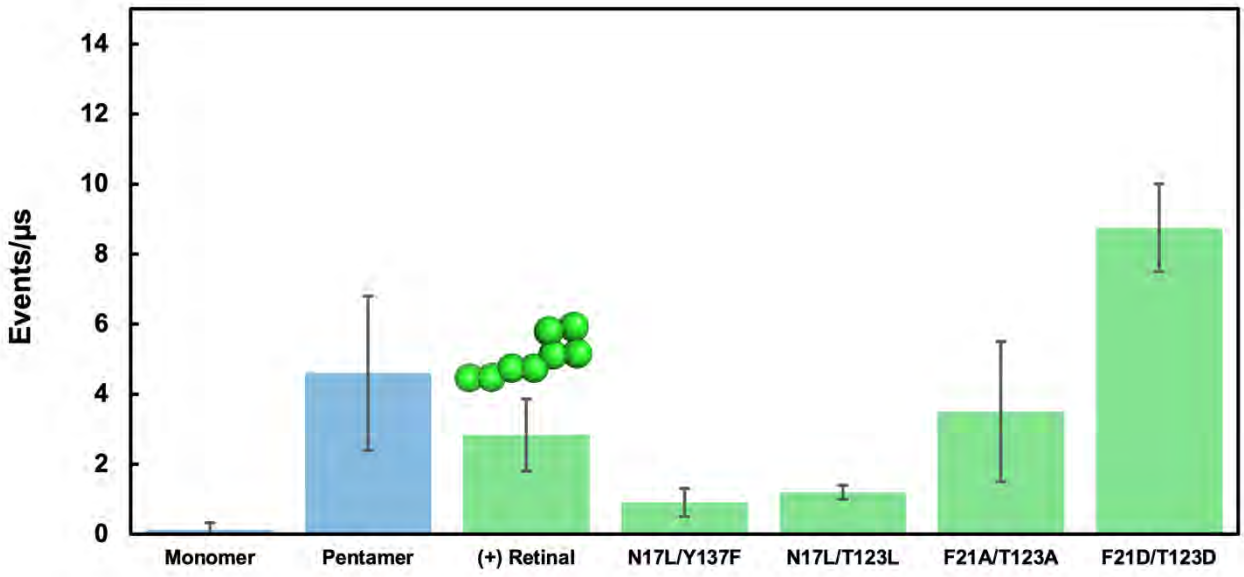

Supplemental Figure 2: CGMD Scramblase Activity Depends on Polar Residues in Protomer Interface. Monomer and pentamer rates are from Figure 2. The coarse-grained bead model for retinal is represented above the bar for scrambling rates with a retinal-bound opsin.

CGMD with retinal

A minimized all-atom pentamer model with retinal was used as the basis for positioning the CG ActR model, thus capturing the coordinates in order to subsequently create a GC retinal model. A python script was used to find centroids every 2-3 beads, 4 in the aliphatic tail and 4 for β-ionone ring of retinal. For bead definitions, SC (small) beads correspond to hydrocarbon backbones and TC (tiny) beads are typically used for rings because they allow for rigidity and tighter packing; the "1" is apolar, and the "2" is slightly more polar (maximum polarity is 4). The first bead of the tail is SC2, and the rest are SC1. All the ring beads are TC1. This approach created a simplified, space-filling model of the retinal ligand rather than a rigorous representation of a conjugated C20 ligand. During GROMACS production runs, a "pull-code" was used to keep the retinal ligands in place. This approach uses harmonic restraints between the centers of mass of two atoms to maintain a specified distance between them. Strong forces of 8000 kj/(mol*nm) were applied between bead 1 of the tail and the side chain bead of lysine 233, with a weaker force of 500 kj/(mol*nm)

between Gly136 and one side of the ring. Subsequent setup and MD runs and scramblase event counting were carried out as described in the main methods section. Result is the average of 3 x 2 μsec MD simulations.

CGMD with amino acid substitutions

The variant opsins were created by substituting side chains in PyMol, followed by vacuum minimization and subsequent steps as described in main text except that the membrane contained 800 DOPC molecules rather than 1000. All variants were tested in two independent runs with consistent outputs.

We designed three kinds of amino acid variants. First, in order to directly test the hypothesis that polar residues in the interface were important for interaction with the phospholipid head group we made two models that each had two amino acid substitutions in the scrambling cleft, from polar to non-polar side chains but of similar size. In one case the positions were at the top and bottom of the cleft on opposing subunits (N17L/T123L) and in the other both were at the top of the cleft, again on opposite faces (N17L/Y137F). Both of these reduced scrambling to <1 event/ μsec (**Suppl. Fig. 2**). As a check that not all substitutions would inhibit scrambling, two models were made with modest substitutions to alanine. In a double mutant (F21A/T123A) rates were not changed significantly. In a triple mutant (Y32A/Y93A/Y137A) scrambling was slightly higher; perhaps three substitutions compromise normal oligomer packing. Finally, introduction of two acidic side chains was tested (F21D/T123D), with an increase in scrambling rate. In our simplistic coarse-grained, implicit solvent model we neutralized each of these Asp residues by setting their charge to 0 in the parameter file and using the P2 polar bead type, reasoning that Asp side chains buried within the lipid bilayer have a higher pKa than those exposed to aqueous solvent. 10 Na+ beads were deleted to accommodate and balance the charge of the system. Future research might explore whether the higher apparent pKa of the carboxylic acid side chains within the membrane keeps these polar side chains protonated (uncharged) and, as a consequence, they may not repel the phosphate head groups but pull them through the cleft.

Reference

1. Morizumi T, Ou W-L, Van Eps N, Inoue K, Kandori H, Brown LS, Ernst OP. 2019. X-ray Crystallographic Structure and Oligomerization of Gloeobacter Rhodopsin. Sci Rep 9:11283.